THz driven field emission: energy and time-of-flight spectra of ions

M Karam, Jonathan Houard, G Damarla, Loic Rousseau, Onkar Bhorade, Angela Vella

PAPER • OPEN ACCESS

THz driven field emission: energy and time-of-flight spectra of ions

IOP Publishing New J. Phys. 25 (2023) 113017 https://doi.org/10.1088/1367-2630/ad0855

New Journal of Physics
The open access journal at the forefront of physics

Deutsche Physikalische Gesellschaft DPG
IOP Institute of Physics

Published in partnership with: Deutsche Physikalische Gesellschaft and the Institute of Physics

OPEN ACCESS

RECEIVED
6 July 2023

REVISED
19 October 2023

ACCEPTED FOR PUBLICATION
31 October 2023

PUBLISHED
13 November 2023

PAPER

THz driven field emission: energy and time-of-flight spectra of ions

M Karam, J Houard, G Damarla, L Rousseau, O Bhorade and A Vella*

Univ Rouen Normandie, INSA Rouen Normandie, CNRS, Normandie Univ, GPM UMR 6634, F-76000 Rouen, France
* Author to whom any correspondence should be addressed.

E-mail: angela.vella@.univ-rouen.fr

Keywords: THz monocycle, atom probe tomography, field emission, field evaporation

Supplementary material for this article is available online

Abstract

We present an experimental and numerical study of ion field evaporation from LaB_6 nanotips using single-cycle terahertz (THz) transients and a static bias voltage. Varying the amplitude and phase of the THz pulses and the value of the bias, we explore the THz-induced reshaping of the ions energy and their time-of-flight spectra. These results prove that short THz transient of about 1 ps can induce ionization and emission of ions from LaB_6 samples by a field effect: the THz transient acts as an ultra-short electrical pulse. Moreover, comparing numerical and experimental results, we prove that the response time of surface atoms to the THz transient is shorter than 1 ps, corresponding to the vibration times of acoustic phonons in LaB_6.

1. Introduction

Controlling electric charges with external terahertz (THz) fields is at the heart of modern physics and has already enabled several advances in nanoscience such as the implementation of THz-driven scanning tunneling microscopy (Jelic *et al* 2017, Yoshida *et al* 2019) and the control of electron field-emission by coupling intense THz pulses to metallic nanostructures (Wimmer *et al* 2014, Li and Jones 2016, Houard *et al* 2020). The extension of this concept to the emission of heavy ions via field-emission (field-evaporation) has been demonstrated very recently by our group thus offering unprecedented possibilities for the control of ions dynamics and their use for matter analysis and manipulation (Vella *et al* 2021). Thanks to high intensity ultrafast lasers, different processes, such as photoconductive antenna (Tani *et al* 1997, Salem *et al* 2005), optical rectification in crystals (Fülöp *et al* 2010, Vicario *et al* 2014), or plasma generation in fluids (Bartel *et al* 2005, Dey *et al* 2017), can be used to create pulsed sources of strong THz field (kV cm^{-1}). These pulses can be enhanced through coupling with nanoscale object for different applications (Liu *et al* 2012, Iwaszczuk *et al* 2015).

We coupled a THz source based on two color plasma generation in air with the atom probe tomography (APT) to control the field emission of ions. In APT, surface atoms are removed one by one by field emission from sharp tips with an end radius of around 50 nm submitted to a DC voltage of several kilovolts and an electrical or a laser pulse (Blavette *et al* 1999, Gault *et al* 2006, Miller and Forbes 2014, Lefebvre-Ulrikson *et al* 2016). The chemical nature of the evaporated ions is determined by time of flight (ToF) mass spectrometry. This technique is thoroughly used with excellent results in material science to study very fine nanostructures in metals and alloys. The possibility of using laser pulses in the visible and ultraviolet domain (UV) opened APT to low-conductive materials such as oxides, semiconductors or biomaterials (Lefebvre-Ulrikson *et al* 2016, Arnoldi *et al* 2018, Grandfield *et al* 2022).

Intense THz pulses have achieved non-thermal field evaporation in the case of metallic materials, where the THz field is enhanced by the metallic antenna effect (Houard *et al* 2020, Vella *et al* 2021). These recent achievements prove that this new approach relies on a set of physical phenomena and processes that are different from those usually involved in field-emission of ions by UV laser pulses (e.g. light absorption, energy transfer to the sample, thermal assisted evaporation, etc).

The observation of a non-thermal evaporation of ions using THz pulses is a major advancement for the APT application since, to preserve the spatial resolution of the APT images and increase its sensitivity, all the thermal processes should be minimized. However, as for electrical pulses, the THz pulses can induce energy deficit or energy gain on the field-emitted ions, which will impact the mass resolution of the instrument, as previously reported for longer electric pulses (Rousseau *et al* 2020).

Here we present the numerical calculations of the ions trajectories under the action of the static DC field and the THz transient and we study the effect of the THz pulse characteristics, in terms of amplitude and phase, on their ToF. By comparing with experimental results on refractory ceramic materials such as LaB_6, we prove that very short THz pulses can induce the athermal evaporation of ions and can control their kinetic energy.

The article is organized as follows: in the first section, we make a short overview of the field evaporation model, in the second (third) section we present the numerical (experimental) methods and results, respectively. In the last section, our discussions and conclusions are drawn.

2. Theoretical considerations

When a positive electric field of several volts per angstrom is applied on a metal surface, surface atoms evaporate in the form of ions.

In the absence of an applied field, the energy required to remove an atom from the specimen surface as a positive ion of charge state n is called the desorption energy Q_0 and it is proportional to the heat of sublimation Λ of the material. In the presence of an external field, the ionic states become more stable as the distance from the metal surface is increased. The value of the ionic potential energy at this maximum position is known as the 'Schottky hump' $V_{\max}$.

The activation energy Q_n, i.e. the difference between the atomic and ionic potential energies is given by

$$Q_n = -\left(\Lambda - V_{\max}\right). \tag{1}$$

Its dependence on the electric field can be simplified as:

$$Q_n = C\left(1 - \frac{F}{F_{\text{evap}}}\right) \tag{2}$$

where F_{evap} is the evaporation field, it means the field which cancels the activation energy barrier and C is the asymptotic zero field energy of the activation energy, typically ranging from 0.2 eV to 1 eV (Kellogg 1984).

The rate of the evaporation process is given by the Arrhenius equation:

$$\phi\left(s^{-1}\right) = \nu \exp\left(-Q_n/k_{\text{B}}T\right) N_{\text{king}} \tag{3}$$

where ν is the vibration frequency of surface atoms, k_{B} the Boltzmann constant, T the emitter temperature and N_{king} the number of atoms in the position of highest field. The evaporation time at $F \approx F_{\text{evap}}$ is given by the inverse of the vibration frequency of surface atoms $\tau_{\text{evap}} = 1/\nu$, typically a few picoseconds (Kellogg 1984). This means that if the potential atomic barrier oscillates too fast as compared to the typical evaporation time τ_{evap}, the surface atoms will see the mean value of the barrier on the time τ_{evap}. For (100) oriented LaB_6 the transverse and longitudinal acoustic phonons have a frequencies between 1 and 3 THz, corresponding to times ranging from 0.3 to 1 ps (Smith *et al* 1985).

3. Numerical methods and results

3.1. Numerical methods

We use a commercial particle trajectory analysis software LORENTZ-2E V10.2 to model the flight path ions in the home-made atom probe chamber. In our previous work (Vella *et al* 2021) we used simplified model based on a static field as a superposition of a homogeneous long range component and a more confined component with a near-field dipole decay length equal to the tip apex-radius. Here we want to move away from this simplification and calculate the real variation of the electric field from the tip to the detector.

The chamber is represented as an X-axisymmetric structure and the tip is modeled as a cone with a semi-circular apex of r = 70 nm and an angle of 87°, as shown in figure 1(a). The tip is biased at a constant DC voltage (V_{DC}) of a few kilovolts in addition to a monocycle THz pulse. The monocycle is defined mathematically as:

$$V_{\text{THz}}(t) = A\cos\left(\omega\left(t - t_0\right) + \phi\right) \exp^{-\frac{(t-t_0)^2}{\sigma^2}}, \tag{4}$$

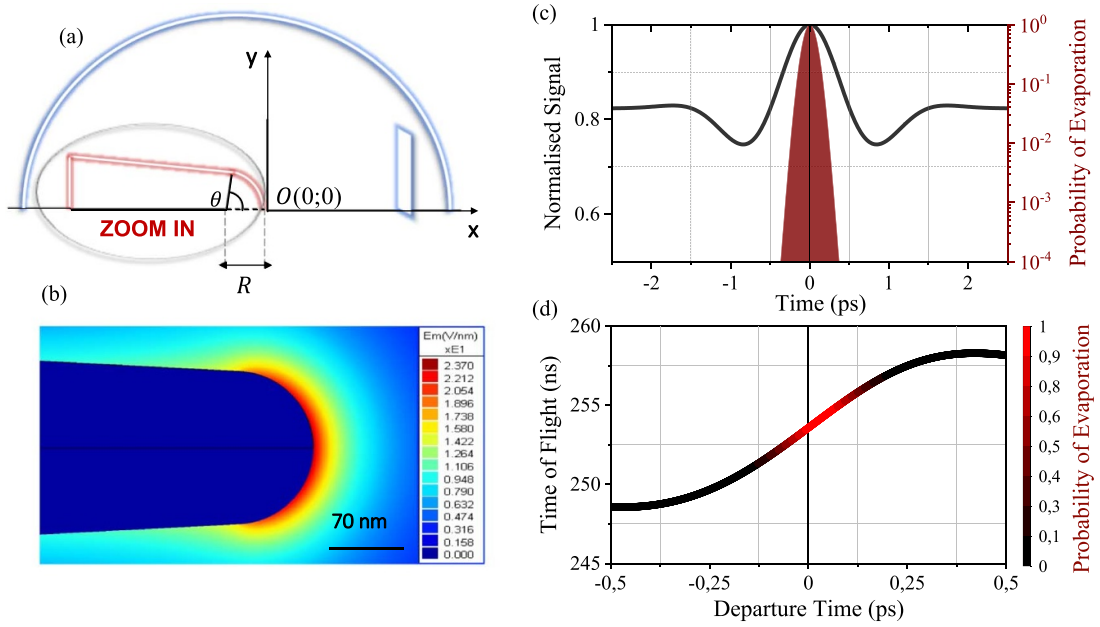

Figure 1. (a) Schematic representation of the APT chamber: the surface in blue are grounded, in red at the potential $V(t)$. The tip in presented with a zoom in. (b) Electric field distribution for $V_{DC} = 7$ kV and the THz pulse amplitude $A = 4.5$ kV. (c) Representation of the total potential $V(t)$ and the associated evaporation probability for $C = 0.4$ eV. (d) The calculated ToF spectra for B^{2+} ions for $V_{DC} = 7$ kV and the THz pulse amplitude $A = 4.5$ kV, the phase $\phi = 0$ and the frequency $\omega = 3.14$ THz.

where A represents the amplitude of the THz pulse, ω is its frequency, and ϕ the phase. While t_0 and σ correspond respectively to the time of the maximum of the pulse and the pulse duration. The MCP detector was illustrated as a flat panel that measures 4 cm in height and it is grounded such as the hemispherical shield of radius 15 cm. Then, following the experimental setup properties, we fixed the tip-to-detector distance at $L = 9$ cm.

The LORENTZ-2E software solves the Laplace equation ($\nabla^2 V = 0$) in the simulation space, by using the boundary element method in quasi-transient mode. It means that the simulation space is discretized into cells and the electrical potential is calculated in each cell at each time step, taking into account the boundary conditions, in particular the variation in time of the tip potential (see equation (4)).Therefore, the problem is considered as a sequence of steady-state problems. Then, for each time step, the electric field is calculated throughout the simulation space by calculating the gradient of the electric potential ($\vec{F} = -\vec{\nabla} V$). An adaptive mesh was used to discretize the space with a smaller mesh size near the sample apex. The field around the apex is shown in figure 1(b). To calculate the trajectory of the ions, we define the properties of the emitted ions, i.e. their mass (m), charge (ne), start position $O(0,0)$, the initial velocity (0,0,) and departure time and we use a fifth-order adaptive step Runge–Kutta (RK5) algorithm to solve the dynamic equation ($m\vec{a} = ne\vec{F}$), in order to calculate the trajectories of the emitted ions. This algorithm takes into account the variations in time and space of the electric field to accurately determine their trajectories. In summary, for each departure time, we got the time of flight, the velocity, the position of detection and the electric field perceived by each ion.

We evaluated the ToF as a function of departure time. As shown in the figure 1(c), for each departure time, a given probability of evaporation was calculated according to the Arrhenius law of equation (3), where the activation energy is given by equation (2) with F/F_{evap} replaced by $V(t)/V_{max}$ with $V(t) = V_{DC} + V_{THz}$, V_{max} its maximum value and C = 0.4 eV. Then, the ToF was calculated following the methodology reported in Rousseau *et al* (2020).

3.2. Kinetic energy of the ions

From the value of the final velocity of ions we can calculate their kinetic energy as a function of the departure time. For ions having a small mass-on-charge-ratio (MCR), lower than 15 amu, the kinetic energy follows the behaviour of the THz pulse (potential energy) with a negative phase shift (see figure 2(a)). In fact, ions emitted before the maximum of the THz pulse are accelerated, however ions emitted after the maximum are decelerated, compared to the energy they can acquire thanks only to the static DC voltage. For large MCR ions the kinetic energy shows a shape different from that of the potential energy and ions experience a light acceleration or deceleration compared to small MCR ions (see figure 2(b)). This different behaviour can be

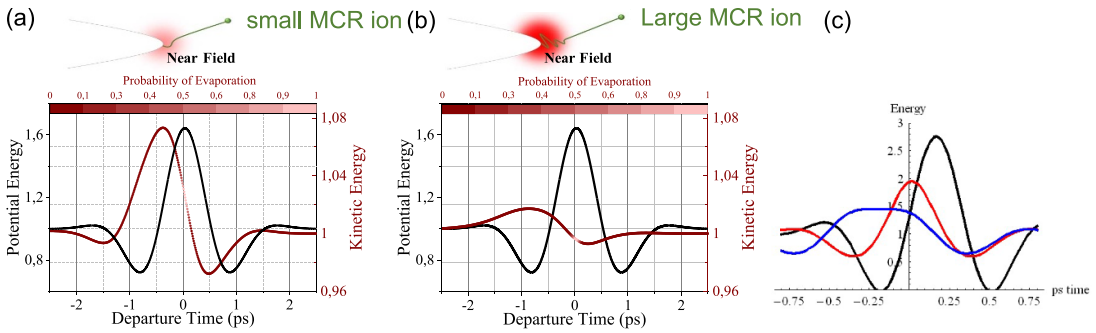

Figure 2. Kinetic energy of (a) B^{2+} ions and (b) La^{2+}, for a $V_{DC} = 7$ kV and a THz pulse amplitude $A = 4.5$ kV. (c) Analytical calculation of the kinetic energy (in arbitrary unit) following equation (5), for $t_{out} = 0.3$ ps (red line) and 0.7 ps (blue line), black line represents the potential energy.

explained considering the time that small and large MCR ions need to travel the region of high electric field, where they can feel the action of the THz transient. For small MCR ions, this time is short enough to experience only a part of the THz transient, however large MCR ions travel for a longer time and will feel all the variation of the THz pulse, as shown in the schematics of figures 2(a) and (b). In a first approximation, we can consider the electric field constant in the near field region and compute the momentum of the ions by the temporal integral over the field:

$$mv(t_{start}) = \int_{t_{start}}^{(t_{start}+t_{out})} F(x=0,t)\,dt, \tag{5}$$

with t_{start} the departure time of the ion and t_{out} the travel time in the high-field region. Then the kinetic energy will be $E_k \propto v(t_{start})^2$.

As reported in figure 2(c), for a t_{out} of 0.3 ps and 0.7 ps we reproduce the kinetic energy behaviour of the small and large MCR ions, respectively. For each ion, the value of t_{out} corresponds to the time required to travel a distance of 10 nm from position $(0,0)$. At this distance the value of the electric field is reduced by 25% compared with its value at position $(0,0)$.

Note that the change in the static voltage will change the travel time of ions in the high field region and can hence affect the kinetic energy of ions, as will be discussed in the following section.

3.3. Effect of the THz pulse amplitude and phase

The calculation of ToF spectra were performed for two different values of the phase of the THz pulse: $\phi = 0$ and $\phi = \pi$ in order to have a positive and a negative THz pulse. The frequency of the THz pulse was fixed at $\omega = 3.14$ THz.

For positive pulses, the static potential was fixed at 7 kV and the amplitude of the THz pulse was increased from 3 kV to 13 kV, as shown in figures 3(a) and (b). The small MCR ions (such as B^+) are accelerated and the large MCR ions (such as La^{2+}) are decelerated by the THz pulse for all the values of the pulse amplitude. However, the acceleration and deceleration are stronger when the amplitude of the THz transient is increased. Moreover, the width of all the ToF peaks increases with the THz amplitude, and the shape of the peaks evolves from a symmetric towards an asymmetric shape, showing a tail on the right, for small MCR ions, and on the left, for large MCR ions.

To better compare numerical and experimental results, we calculate the ToF resolution (R) for each peak as the ratio between the width of the peak @ 1/100 of its maximum (ΔToF) and the value of the ToF at the maximum of the peak (ToF_{max}): $R = \frac{ToF_{max}}{\Delta ToF}$. Figure 4(a) shows the variation of the inverse of R as a function of the THz amplitude for four values of MCR at a fixed voltage of 7 kV. A linear dependence is observed for all MCRs and the date are fitted using the function:

$$\frac{\Delta ToF}{ToF_{max}} = a(MRC, V_{DC})A + b(MCR, V_{DC}), \tag{6}$$

are also represented. The constant b varies as a function of MCR and V_{DC} because:

$$b(MCR, V_{DC}) = \frac{\Delta_{det}}{ToF_0}, \tag{7}$$

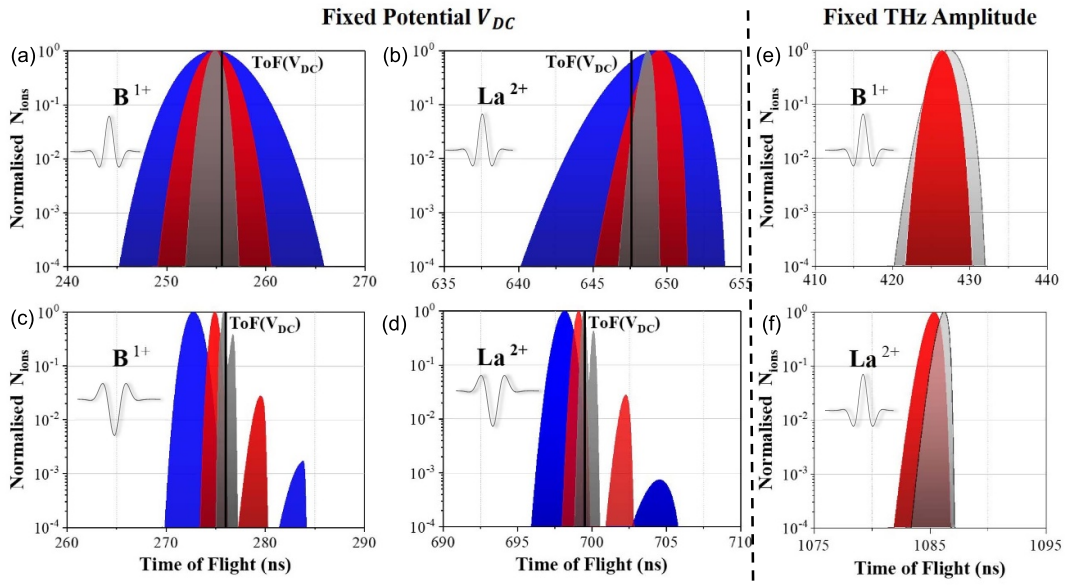

Figure 3. (a), (b) Calculated ToF for positive THz pulses at $V_{DC} = 7$ kV varying the THz amplitude (A) for B^+ ions and La^{2+}, respectively: blue $A = 13$ kV; red $A = 7$ kV and grey $A = 3$ kV. (c), (d) Calculated ToF for negative THz pulses at $V_{DC} = 6$ kV varying the THz amplitude (A) or B^+ ions and La^{2+}, respectively: blue $A = 7.5$ kV, red $A = 3$ kV and gray $A = 0.6$ kV. (e), (f) Calculated ToF for positive THz pulses with $A = 3$ kV varying the Dc voltage for B^+ ions and La^{2+}, respectively: red $V_{DC} = 8$ kV and grey $V_{DC} = 2.5$ kV.

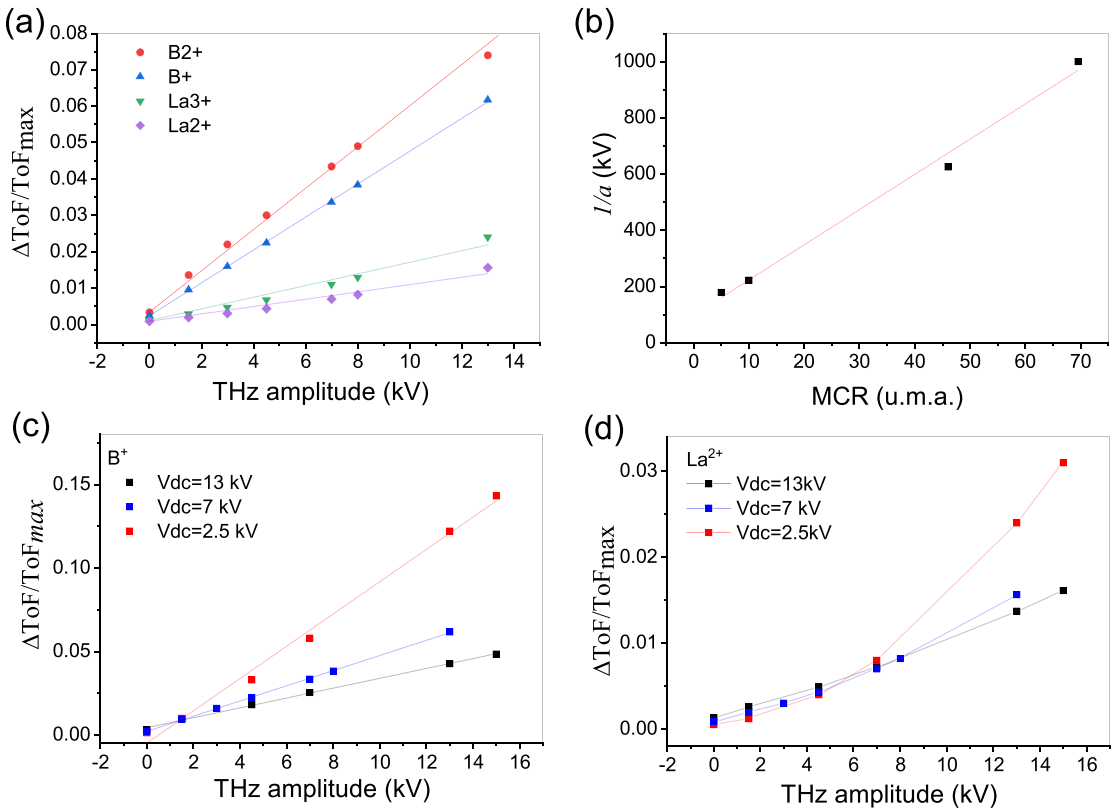

Figure 4. (a) Calculated $\Delta ToF/ToF_{max}$ for positive THz pulses at $V_{DC} = 7$ kV as a function of the THz amplitude for B^{2+}, B^+, La^{3+} and La^{2+} ions. Full lines correspond to the linear fit of the data. (b) The inverse of the slopes of the linear regression fit of (a) as function of MCR of the ions. (c), (d) Calculated $\Delta ToF/ToF_{max}$ for positive THz pulses as a function of the THz amplitude, for three values of the DC voltage, for B^+ and La^{2+}, respectively.

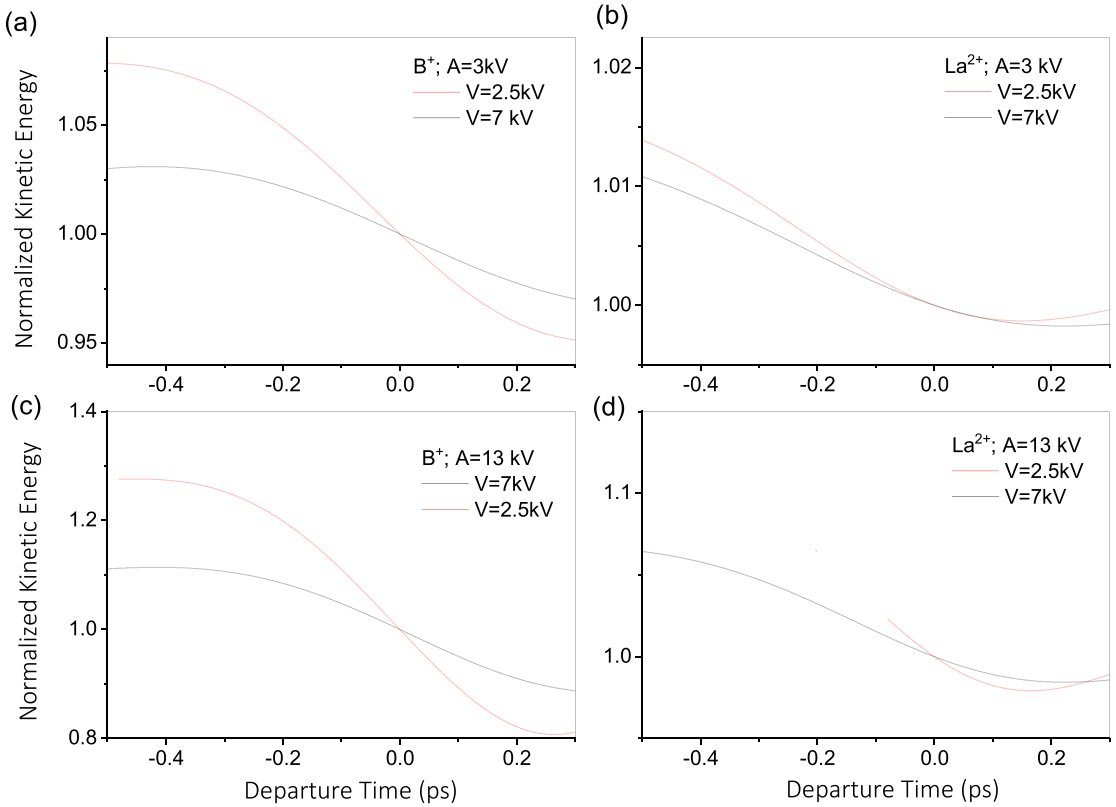

Figure 5. Kinetic energy of (a)–(c) B^+ ions and (b)–(d) La^{2+} ions, for a $V_{DC} = 2.5$ nad 5 kV and a THz pulse amplitude $A = 3$ kV for (a), (b) and $A = 13$ kV for (c), (d).

where Δ_{det} is the width of the detector response at 1/100 of its maximum: Δ_{det} =0.6 ns, and ToF_0 is the ToF when the THz amplitude is zero. For ions emitted by a static field, from the energy conservation low, we know that $\frac{1}{2}m\frac{L^2}{\mathrm{ToF}_0^2} = neV_{DC}$, so that $\mathrm{ToF}_0 = \sqrt{\frac{L^2 \times \mathrm{MCR}}{2V_{DC}}}$. Therefore equation (7) becomes:

$$b(\mathrm{MCR}, V_{DC}) = 0.6\sqrt{\frac{2V_{DC}}{L^2 \times \mathrm{MCR}}}. \tag{8}$$

The inverse of the slope $a(\mathrm{MCR}, V_{DC})$ varies linearly as a function of MCR, as reported in figure 4(b). Note that the ΔToF as a function of the THz amplitude (A) changes little with the MCR (see supplementary informations). Therefore, the dependence of the time resolution on the MCR is mainly due to the variation of ToF_{max}. with the MCR of ions. Without THz pulse ($A = 0$), the $\mathrm{ToF}_{max} = \mathrm{ToF}_0 \propto \sqrt{\mathrm{MCR}}$. The THz pulse straights this dependence because ToF_{max} is reduced for small MCRs and increased for large MCRs, as shown in figures 3(a) and (b). This effect is known as the dynamical effect and it was already reported for ions in APT having accelerating electrodes (Rousseau *et al* 2020).

For negative pulses, the static potential was fixed at 6 kV and the amplitude of the THz pulse was increased from 0.6 kV to 7.5 kV. In this case, the ions can be emitted on the two maxima of the THz pulse, therefore we observe double ToF peaks for all the ions and for all the THz amplitudes, as shown in figures 3(c) and (d). Note that we simulate a THz negative pulse with the two maxima having slightly different highs, the lowest one arriving first. The time distance between the two peaks Δt increases linearly with the amplitude: $\Delta t = 1.67A$. Moreover, the ratio between the high of the first and second peak increases. As for positive pulses, the width of the peaks increases with the THz amplitude and their shape changes. Moreover, the ions emitted on the first positive maxima of the THz pulse are always decelerated and the ions emitted on the second positive maxima of the THz pulse are accelerated when the THz amplitude increases.

3.4. Effect of the static DC voltage

For a fixed phase of THz pulse corresponding to a positive pulse, we studied the change induced by the static voltage on the ToF spectra of the ions. First, the behaviour of $\Delta\mathrm{ToF}/\mathrm{ToF}_{max}$ as a function of the THz amplitude changes with the static DC voltage. At low (high) DC voltages the behaviour is nonlinear for large (small) MCR ions, respectively (see supporting information). The figures 4(c) and (d) focus on the variation

of $\Delta ToF/ToF_{max}$ as a function of A for three values of DC voltage for B^+ and La^{2+} ions, respectively. For B^+, a linear behaviour is reported with the inverse of the slope increasing linearly with the voltage (the behaviour is shown in the supplementary informations). For La^{2+}, the behaviour becomes nonlinear at low DC voltage, moreover a cross point is observed at $A = 6$ kV where the dependence of time resolution on DC voltage is reversed. As reported in figure 3(e), for a fixed THz amplitude $A = 3$ kV, increasing the applied potential will reduce the width of ToF peaks of small MCR ions. Note that to compare the ToF spectra obtained for two values of the voltage, we rescaled the ToF following the formula: $ToF_1 = ToF_2\sqrt{\frac{V_{DC2}}{V_{DC1}}}$. The square root factor is obtained considering that, in ToF mass spectrometry, $MCR \propto ToF^2 \times V_{DC}$ and it is constant whatever the value of the potential (Lefebvre-Ulrikson *et al* 2016). As shown in figure 3(f), an opposite behaviour is reported for large MCR ions such as La^{2+}.

We can understand this behaviour looking at the kinetic energy shape reported in figures 2(a) and 5(a). For ions such as B^+, the kinetic energy of ions with a high probability of evaporation decreases linearly as a function of the departure time. The increase of the static voltage will reduce the travel time of ions in the high field region and therefore decrease the acceleration and deceleration of ions. It follows that the slope of the linear decay in kinetic energy decreases. This will result in narrower peaks in the ToF spectrum. This behavior does not change changing the amplitude of the THz transient, as shown in figure 5(c). However, for ions such as La^{2+}, at low THz amplitudes such as 3 kV, ions with a high probability of evaporation have kinetic energy values around the energy minimum, as shown in figures 2(b) and 5(b). The width of the peaks in the mass spectrum will then be a function of the value of the second derivative of the kinetic energy at the minimum. The smaller the second derivative, the narrower the peak. Increasing the voltage will reduce the travel time and also increase the value of this second derivative (see supplementary informations). At high THz amplitudes such as 13 kV, ions with a high probability of evaporation have now energies higher than the energy minimum and the dependence on the DC voltage become similar to that of B^+ ions, as shown in figure 5(d).

4. Experimental methods and results

4.1. Experimental setup

Experiments were performed in a home-made ultrahigh vacuum chamber with a flight path of 10 cm, a base pressure of 5×10^{-11} mbar and a compression cryostat cooling of the sample to 50 K. The sample is polarized with a positive or negative applied DC bias, yielding an intense field at the tip apex. Field ion evaporation can be triggered by the THz pulses or the femtosecond near infrared radiation (NIR) laser pulses. Surface atoms may ionize and leave the surface, flying toward a detector sensitive to the impact position of the ion and to its ToF. The ToF of the ions allows for the identification of their mass/charge ratio, i.e. (with some limitations) of their chemical identity. The position sensitive detector used in this study is a delay line detector with improved multihit capabilities. It consists of a conventional 8 cm Roentdek delay line detector following a pair of microchannel plates (MCP) in chevron configuration. Signal output from each end of the two wire pairs are digitized by means of fast digitizer boards PXI DC 271 from Acquiris. Ion flight time signals are taken as output from the MCP.

Our optical setup relies on THz generation by two-colors ultra-short laser pulse composed of the fundamental harmonic (FH) and its second harmonic (SH). The THz generation is mainly due to the creation of an asymmetric electron current by the photo-ionization and acceleration of electrons from the air or N_2 gas. The produced THz field is characterized by electro-optic (EO) sampling inside a non-linear crystal and then it is focused on the sample inside the APT ultra-vacuum chamber. The optical setup is presented in figure 6.

The laser system is a Spitfire model from Spectra Physics delivering 35 fs pulse in the infrared at 800 nm wavelength with a repetition rate of 1 kHz and a maximum energy of 4 mJ. The FH and the SH of the laser are focused in air to create a plasma. The THz pulse is generated by two-colors-plasma generation in air or N_2 (Bartel *et al* 2005, Kim *et al* 2007, 2008). The NIR laser beam is focused in air by a 40 cm focal lens and pass through a BBO crystal placed before the focal plane, in order to generate the SH at 400 nm. The focused bi-chromatic femtosecond laser pulses emit THz radiation with very high field strengths. The energy of the FH is fixed at 2.65 mJ which corresponds to the intensity of 3×10^{15} W cm^{-2}. At the FH intensity of 3×10^{15} W cm^{-2} the THz generation is mainly due to photoionization of the gas (Andreeva *et al* 2016). The amplitude of the emitted THz pulses can be controlled by changing the aperture diameter and the polarity of the pulse (positive or negative pulse) can be controlled changing the distance of the BBO crystal from the plasma (Kim *et al* 2007). The produced THz field is then focused on the sample inside the APT ultra-vacuum chamber. The THz transient is characterized by EO sampling inside a non-linear crystal (100 μm thick GaP) outside the APT chamber and it can also be characterized in the near field of the nanotip by pump-probe electron emission analysis, using the THz pulse as a pump and the FH of the laser as a probe.

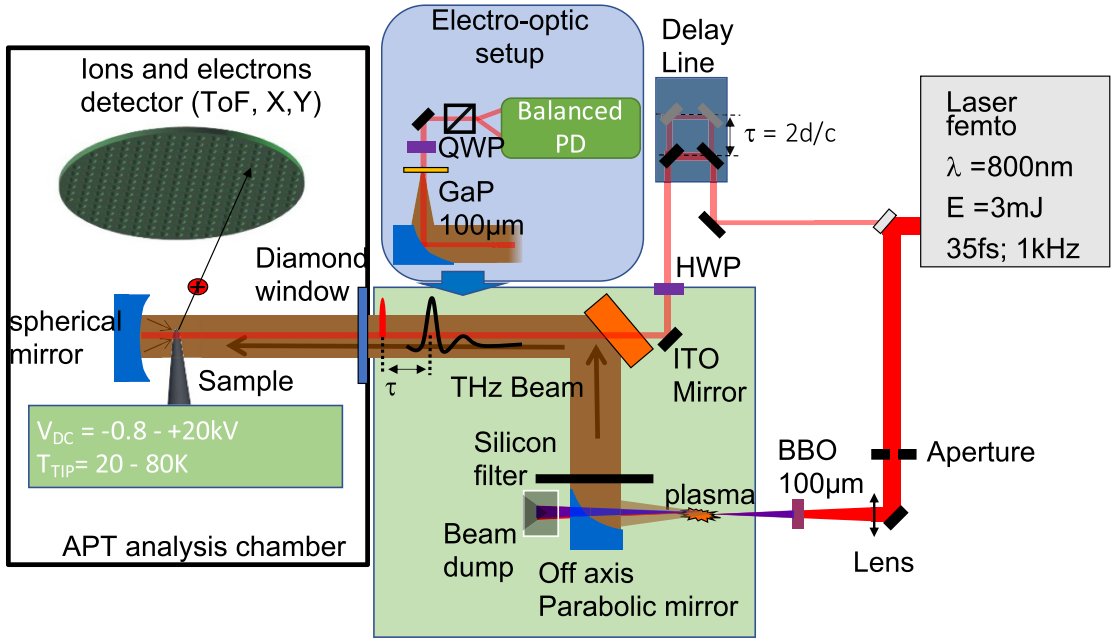

Figure 6. (a) Scheme of the experimental setup: focusing lens ($f = 400$ mm), BBO crystal for SH generation, silicon wafer as NIR filter, ITO mirror: THz mirror, GaP electro-optic crystal, QWP: quartz wave plate. The green area highlights the part of the setup with a gas control.

4.2. THz transient characterization in the near field

The THz field at the apex of the APT sample is measured using this THz field to enhance the photo-electron emission from the sample, in a pump-probe setup where the NIR laser is used as a pump for photo-emission and the THz transient as a probe of the emission rate.

The input power of the FH is attenuated of more than a factor 20 by the use of the aperture (diameter of the aperture of 3 mm) and the BBO position is adjusted in order to generate a negative THz pulse, shown by a red line in figure 7(b). Using a NIR pulse of 12 GW cm^{-2} (12 nJ), the electron photoemission properties of the LaB_6 sample under NIR illumination are measured as a function of the negative bias and presented in figure 7(a).

Then, the negative bias is fixed at 100 V, and the THz pulse is added to the NIR pulse with a variable time delay. The emitted current varies as a function of the delay, following the strength of the THz pulse, as shown in figure 7(c). The THz pulse polarity is changed to positive and the procedure is repeated (black curve in figure 7(c)). The THz signal is recomposed by taking the positive and negative parts, respectively. The last step is the conversion of the emission signal in equivalent voltage. The change in the emission current is compared to the change measured as a function of the bias using only NIR pulse (see figure 7(a)), and the equivalent THz voltage is calculated, see figure 7(d). We observed same deviation from the THz pulse measured by EO sampling, due to the antenna response of the tip (Wang *et al* 2004, Houard *et al* 2020). In particular, the pulse duration is longer, about 1.3 ps compared to 0.5 ps of the EO signal. Note that the amplitude of 700 V corresponds to a FH beam which was attenuated by more than a factor 20.

We converted the measured rectified THz voltage into the near-field using the relation $F = V_{DC}/(kr)$ with k a geometrical factor ranging from 4 to 9 and r the apex radius. To measure the kr factor, we field evaporated the sample biased to 6.3 kV using only NIR laser pulses at $I_{NIRlaser} = 12$ GW cm^{-2}. Following Kingham theory (Kingham 1982), from the ratio of the $La^{3}+/La^{2+}$ peaks in the collected spectrum, we calculated the surface field at 18 V nm^{-1} and, hence, the factor $kr = 0.35 \frac{\text{kV}}{\text{V nm}^{-1}}$. The amplitude of the THz pulse in figure 7(d) is therefore 2 V nm^{-1} (2×10^4 kV cm^{-1}), about 1000 times higher than the incident THz field of 20 kV cm^{-1}, as shown in figure 7(b).

4.3. Sample preparation

We decided to work with LaB_6 samples, because its field evaporations gives rise to B^{2+} and B^{+} ions, small MCR ions, and La^{3+} and La^{2+}, high MCR ions. Moreover, LaB_6 is refractory ceramic material, with metal-like conductivity, and a low emission work function corresponding to one of the highest electron emissivities known.

The LaB_6 field emitter tips are prepared by electrochemical etching in a 10% HNO_3 solution (Wang *et al* 2009). To reduce the end radius of the nanotip we used a dual beam scanning electron microscope (SEM)

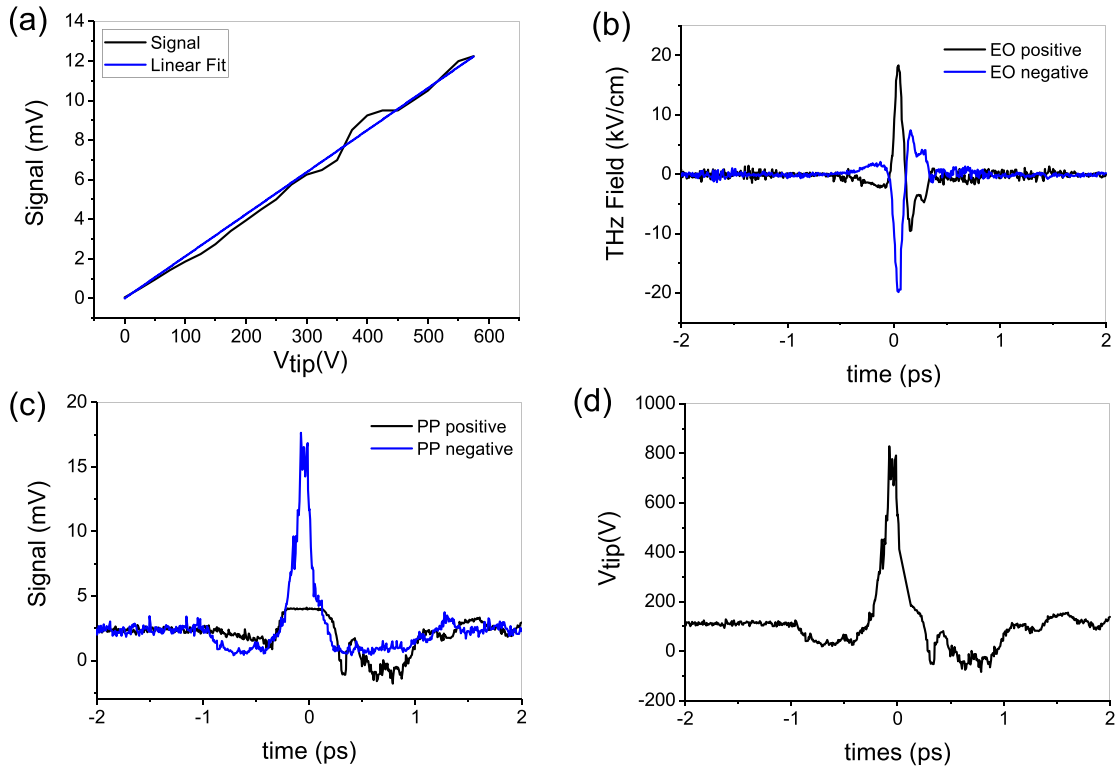

Figure 7. Rectified terahertz voltage at the tip apex. (a) Current–voltage characteristic of electrons emission obtained from an LaB_6 tip under laser illumination at $I_{NIRlaser} = 12\ GW\ cm^{-2}$. (b) Two terahertz transients with inverted field directions (polarity) detected with electro-optic (EO) sampling outside the atom probe chamber with an aperture of 3 mm. (c) Photocurrent modulation for the terahertz waveforms corresponding to the electro-optic traces of (b) and $U_{bias} = -100$ V, $I_{NIRlaser} = 12\ GW\ cm^{-2}$. (d) Rectified terahertz pulse with positive polarity, reconstructed from (a) and (c).

equipped with a focused ion beam. A radius of about 20 nm is achieved by annular milling. With the help of the SEM, the size of the apex and the shank angle are determined with an accuracy of 10 nm. Most of the milling was performed using 30 keV ions, while 12 keV ions were used in the final milling step in order to minimize the presence of defects in the final sample.

4.4. Experimental results

LaB_6 sample were first analysed at low THz amplitude of about 6.5–7.5 kV and high static voltage of 7 kV . The main peaks of the ToF spectrum are reported in figures 8(a) and (b). The increase of the amplitude of the THz pulse of 10% induced an increase of the evaporation rate and of the widths of the peaks, as predicted by numerical simulations. However, we cannot observe the predicted peak asymmetry because a further increase in the THz amplitude will induce a huge evaporation rate which can reduce the performances of the detector and hence increase the ToF peak width. In order to study the effect of high amplitude THz pulses, we reduced the applied voltage to 2.5 kV. The pump energy of the laser was set at its maximum, corresponding to a THz amplitude of about 13.5–15 kV. The figures 8(c) and (d) shows the ToF peaks of B^+ and La^{2+} ions obtained for the full THz amplitude and a reduced amplitude of 10%. Again we can note that the increase in the THz amplitude induces an increase in the peaks width. The asymmetry on the right for B^+ ions and on the left for La^{2+} ions is now well observed. We can also remark that a second peak is visible for B^+. This second peak is due to a delayed emission probably triggered by electrons emitted at the negative values of $V(t)$. These electrons are field emitted and then accelerated back to the sample surface where they can trigger a new emission of ions. This emission mechanisms will be discussed in a future work and it is out of the scope of this article.

For negative THz pulses we worked at high static voltage of 6.6 kV and low THz amplitude of about 2–3 kV. A double peak is visible for B^+ peak, as shown in figure 8(e). The time-distance between the two peaks is of about 1 ns and it slightly increases by increasing the THz amplitude by 10%, meanwhile the relative high decreases, as predicted by numerical simulations. For La^{3+}, only one large peak is observed. We can probably not see the double peak structure as calculated numerically because the time distance is expected to be shorter than 0.7 ns and because we have a lower statistic and hence a worse resolution of the peaks due to the lower content of La in the sample.

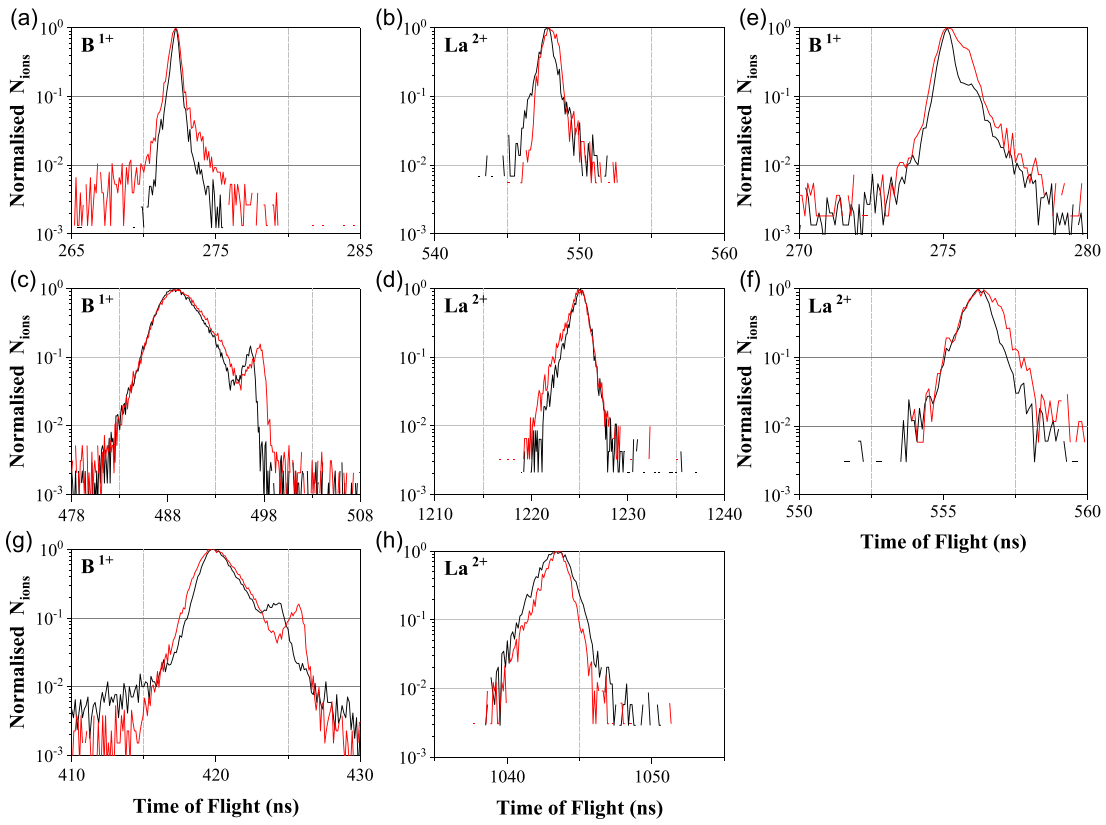

Figure 8. (a), (b) ToF at $V_{DC} = 7$ kV and a positive THz amplitude of about 6.5 (black line) and 7.5 kV (red line), for B^+ and La^{2+} ions, respectively. (c), (d) ToF at $V_{DC} = 2.5$ kV and a positive THz amplitude of about 13.5 (black line) and 15 kV (red line), for B^+ and La^{2+} ions, respectively. (e), (f) ToF at $V_{DC} = 6.6$ kV and a negative THz amplitude of about 2.5 (black line) and 3 kV (red line), for B^+ and La^{2+} ions, respectively. (g), (h) ToF for a positive THz amplitude of about 15 kV and $V_{DC} = 3.2$ (red line) and 5 kV (black line) for B^+ and La^{2+} ions, respectively (Karam M *et al* 2023).

We also changed the potential applied to the sample keeping the THz amplitude at its maximum for a positive pulse. To compare the ToF spectra obtained for two values of the voltage, we rescaled the ToF times following the formula: $\mathrm{ToF}_1 = \mathrm{ToF}_2\sqrt{\frac{V_{DC2}}{V_{DC1}}}$. As shown in figures 8(g) and (h), the width of the B^+ peak decreases when the voltage in increased, as obtained by numerical simulation. For La^{2+} peak, almost no changes are observed with the increase of the potential. Numerically, the increase of the La^{2+} peak's width at 1/100 of its maximum is of about 0.4 ns, by doubling the potential. Experimentally, 0.4 ns is lower than the error bar of the peak-width measurement at 1/100 of its maximum.

5. Discussions and conclusions

From numerical and experimental results we explore the THz-induced change of ion's energy and the following impact on the ToF spectra. Experimental results reproduce well the predictions of the numerical simulations, in terms of expected trends: asymmetry of the ToF peaks, increase of the peak width with the THz amplitude, presence of a double peak for negative THz pulses. This agreement between experimental and numerical behaviours is a proof that LaB_6 samples are evaporated by a field effect assisted by the THz transient. Furthermore, the TOF peaks in figure 8 do not show an asymmetric shape with a long tail, over several hundred nanoseconds on the right-hand side, as is always reported for thermal evaporation. This long tail corresponds to the ions evaporated during the sample cooling process. Consequently, we consider the thermal contribution to be negligible. More details on the thermal evaporation spectra and comparison with THz spectra are available in Supplementary Information.

To compare numerical and experimental results, we look at the ToF resolution for each peak and experimental conditions. For a positive THz pulse, we can use the linear regression of equation (6) to calculate the value of the ratio $\Delta\mathrm{ToF}/\mathrm{ToF}_{max}$, for the each experimental condition, in term of THz amplitude and DC voltage. As shown in figures 9(a) and (b) for B^+ and La^{2+} ions, respectively, the experimental values are always lower than the calculated values. In order to have a good agreement between

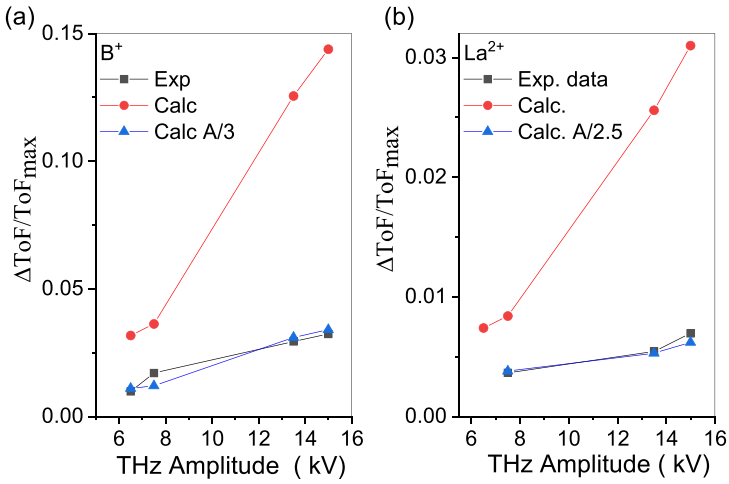

Figure 9. Calculated and experimental data of ΔToF/ToF for B^+ ions (a) and La^{2+} ions (b).

the experimental data and the predictions of equation (6), the value of THz Amplitude used in the calculation have to be reduced by a factor 3 for B^+ ions and by a factor 2.5 for La^{2+}.

Similarly, concerning the results obtained with a negative THz pulse at $V_{DC} = 6.6$ kV, the time-distance ($\Delta t = 1$) ns between the two peaks in the ToF spectrum of B^+ is obtained experimentally for a THz amplitude of about 2 kV and numerically for an amplitude of 0.6 kV. Using the linear function linking Δt to the THZ amplitude, which was obtained by numerical simulation, $\Delta t = 1.67A$, for $\Delta t = 1$ ns the value of A = 0.6 kV is calculated. Therefore, also in this case, the agreement between the calculated and experimental data is found only dividing the experimental values of the THz amplitude by a factor 3. Note that experimentally, the THz amplitude is measured by pump-probe electron emission set-up, therefore the values reported correspond to the THz field amplitude felt by the electrons. Here, it appears that ions feel a lower field of about a factor 3.

During the field evaporation process, the surface atoms will feel the mean value on the barrier on the evaporation time τ_{evap}, therefore to take into account this response time of the system, we can convolute the function $V(t)$ with an exponential decay function of decay time τ_{evap}. This convolution will change the temporal shape of the THz transient and will attenuate it by a factor depending on the value of τ_{evap}. To get the factor 2.5–3, observed experimentally, the τ_{evap}, should range between. 0.6 and 0.7 ps. The dispersion curves of transversal and longitudinal acoustic phonons in LaB_6 shows frequencies ranging from 1 and 3 THz it means vibrations times ranging between 0.3 and 1 ps (Smith *et al* 1985). Hence, we can conclude that the vibration time of surface atoms under strong electric field is not increased by the electric field, as calculated by *ab-initio* methods in Karahka and Kreuzer (2015) for ZnO samples. In fact, for LaB_6, *ab-initio* calculations show an increase of less than 10% of the phonon frequency with a high pressure of about 10 GPa (Chao *et al* 2016). In APT the huge electric field induces a strain pressure of less than 10 GPa which can explain why we are not able to measure a phonon frequency shift under high electric field (Rigutti *et al* 2017).

In conclusion our results show that surface ions can be field evaporated by a short THz transient, with an oscillation time of about 1 ps, by a non-thermal process. The THz transient acts as an ultra-short electric pulse and modifies the kinetic energy of ions.

By comparing experimental and numerical ToF behaviour, the response time or evaporation time of the surface atoms under high DC field was estimated. This study leads to many experimental and technical advancements. It validates the use of short THz transients to trigger ions emission and, since thermal effects are reduced, the spatial resolution of the APT images is preserved. Moreover, concerning the sensitivity of the instrument in terms of chemical species resolution, which is linked to the ToF resolution R, the energy dispersion is smaller than what was reported using longer electrical pulses and can be corrected using well-known energy compensator electrostatic devices (Lefebvre-Ulrikson *et al* 2016, Rousseau *et al* 2020).

Data availability statement

The data that support the findings of this study will be openly available following an embargo at the following URL/DOI: https://zenodo.org/record/8382828. Data will be available from 06 February 2024.

Acknowledgments

The research leading to these results has received funding from European Union under Grant Agreement No. 101046651. This work was supported by the Regional Council of Normandie.

The data that support the findings of this study are available from the corresponding author upon reasonable request

ORCID iD

A Vella https://orcid.org/0000-0003-1501-159X

References

Andreeva V *et al* 2016 *Phys. Rev. Lett.* **116** 063902
Arnoldi L, Spies M, Houard J, Blum I, Etienne A, Ismagilov R, Obraztsov A and Vella A 2018 *Appl. Phys. Lett.* **112** 143104
Bartel T, Gaal P, Reimann K, Woerner M and Elsaesser T 2005 *Opt. Lett.* **30** 2805–7
Blavette D, Cadel E, Fraczkiewicz A and Menand A 1999 *Science* **286** 2317–9
Chao L, Bao L, Wei W, Tegus O and Zhang Z 2016 *J. Alloys Compd.* **672** 419–25
Dey I *et al* 2017 *Nat. Commun.* **8** 1–7
Fülöp J, Pálfalvi L, Almási G and Hebling J 2010 *Opt. Express* **18** 12311–27
Gault B, Vurpillot F, Vella A, Gilbert M, Menand A, Blavette D and Deconihout B 2006 *Rev. Sci. Instrum.* **77** 043705
Grandfield K, Micheletti C, Deering J, Arcuri G, Tang T and Langelier B 2022 *Acta Biomater.* **148** 44–60
Houard J, Arnoldi L, Ayoub A, Hideur A and Vella A 2020 *Appl. Phys. Lett.* **117** 151105
Iwaszczuk K, Zalkovskij M, Strikwerda A C and Jepsen P U 2015 *Optica* **2** 116–23
Jelic V, Iwaszczuk K, Nguyen P H, Rathje C, Hornig G J, Sharum H M, Hoffman J R, Freeman M R and Hegmann F A 2017 *Nat. Phys.* **13** 591–8
Karahka M and Kreuzer H 2015 *Ultramicroscopy* **159** 156–61
Karam M, Houard J, Darmala G, Bhorade O and Vella A 2023 THz driven field emission: energy and time-of-flight spectra of ions (DATASET) (Version 1) (Zendo) (https://doi.org/10.5281/zenodo.8382828)
Kellogg G L 1984 *Phys. Rev.* B **29** 4304
Kim K Y, Glownia J H, Taylor A J and Rodriguez G 2007 *Opt. Express* **15** 4577–84
Kim K Y, Taylor A, Glownia J and Rodriguez G 2008 *Nat. Photon.* **2** 605–9
Kingham D 1982 *Surf. Sci.* **116** 273
Lefebvre-Ulrikson W, Vurpillot F and Sauvage X 2016 Time-of-flight mass spectrometry and composition measurements. In Atom probe tomography (Academic Press) pp 123–54
Li S and Jones R 2016 *Nat. Commun.* **7** 1–7
Liu M *et al* 2012 *Nature* **487** 345–8
Miller M and Forbes R 2014 *Atom–Probe Tomography: The Local Electrode Atom Probe* (Springer)
Rigutti L, Venturi L, Houard J, Normand A, Silaeva E, Borz M, Malykhin S, Obraztsov A and Vella A 2017 *Nano Lett.* **17** 7401–9
Rousseau L, Normand A, Morgado F F, Stephenson L, Gault B, Tehrani K and Vurpillot F 2020 *Micros. Microanal.* **26** 1133–46
Salem B, Morris D, Aimez V, Beerens J, Beauvais J and Houde D 2005 *J. Phys.: Condens. Matter* **17** 7327
Smith H, Dolling G, Kunii S, Kasaya M, Liu B, Takegahara K, Kasuya T and Goto T 1985 *Solid State Commun.* **53** 15–19
Tani M, Matsuura S, Sakai K and Nakashima S-I 1997 *Appl. Opt.* **36** 7853–9
Vella A, Houard J, Arnoldi L, Tang M, Boudant M, Ayoub A, Normand A, Da Costa G and Hideur A 2021 *Sci. Adv.* **7** eabd7259
Vicario C, Monoszlai B and Hauri C P 2014 *Phys. Rev. Lett.* **112** 213901
Wang K, Mittleman D M, van der Valk N C and Planken P C 2004 *Appl. Phys. Lett.* **85** 2715–7
Wang X, Jiang Y, Lin Z, Qi K and Wang B 2009 *J. Phys. D: Appl. Phys.* **42** 055409
Wimmer L, Herink G, Solli D R, Yalunin S V, Echternkamp K and Ropers C 2014 *Nat. Phys.* **10** 432–6
Yoshida S, Hirori H, Tachizaki T, Yoshioka K, Arashida Y, Wang Z H, Sanari Y, Takeuchi O, Kanemitsu Y and Shigekawa H 2019 *ACS Photonics* **6** 1356–64